

Long-term evolution of double white dwarf binaries accreting through direct impact

Kyle Kremer

Center for Interdisciplinary Exploration and Research in Astrophysics (CIERA)

Department of Physics and Astronomy

Northwestern University, 2145 Sheridan Road, Evanston, IL 60208

`kremer@u.northwestern.edu`

and

Jeremy Sepinsky

Department of Physics and Electrical Engineering, The University of Scranton

Scranton, PA 18510

`jeremy.sepinsky@scranton.edu`

and

Vassiliki Kalogera

Center for Interdisciplinary Exploration and Research in Astrophysics (CIERA)

Department of Physics and Astronomy

Northwestern University, 2145 Sheridan Road, Evanston, IL 60208

`vicky@northwestern.edu`

ABSTRACT

We calculate the long-term evolution of angular momentum in double white dwarf binaries undergoing direct impact accretion over a broad range of parameter space. We allow the rotation rate of both components to vary, and account for the exchange of angular momentum between the spins of the white dwarfs and the orbit, while conserving the total angular momentum. We include gravitational, tidal, and mass transfer effects in the orbital evolution, and allow the Roche radius of the donor star to vary with both the stellar mass and the rotation rate. We examine the long-term stability of these systems, focusing in particular on those systems that may be progenitors of AM CVn or Type Ia Supernovae. We find that our analysis yields an increase in the predicted number of stable systems compared to that in previous studies. Additionally, we find that by properly accounting for the effects of asynchronism between the donor and the orbit on the Roche-lobe size, we eliminate oscillations in the orbital parameters which are found in previous studies. Removing these oscillations can reduce the peak mass transfer rate in some systems, keeping them from entering an unstable mass transfer phase.

Subject headings: Celestial mechanics, Stars: Binaries: Close, Stars: Mass Loss, Accretion, Methods: Numerical

1. Introduction

Binary systems containing compact objects are of great interest in a variety of areas in astrophysics. Of particular importance are double white dwarf (DWD) binary systems where both components are white dwarfs, which may make up the largest fraction of close binary stars (Marsh et al. 1995).

Following common envelope evolution, DWD binaries may emerge with a sufficiently small semi-major axis, allowing gravitational radiation to drive the stars closer together on an astrophysically interesting time scale. These close DWD systems are of prime importance as low-frequency gravitational-wave sources (Hils, Bender and Webbink 1990; Hils and Bender 2000; Nelemans et al. 2001) as well as progenitors of Type Ia Supernovae (Maoz et al. 2014).

As energy loss due to gravitational waves drives the degenerate components of a DWD binary together, it is possible for the system to enter into a stable semi-detached state, in which the less massive component will fill its Roche lobe and begin transferring matter to its companion. Such systems may result in the formation of AM CVn (Nather et al. 1981; Tutukov and Yungelson 1996; Nelemans et al. 2001), which have extremely short orbital periods. During mass transfer, a stream of matter is pulled from the donor star through the inner Lagrangian point. If the matter stream does not impact the surface of the companion star, then the mass lost from the donor is expected to settle into a disc (Frank, King and Raine 2002). Torques exerted between the discs and the component white dwarfs allow angular momentum stored in the disc to be transferred back to the orbit (Soberman et al. 1997; Frank, King and Raine 2002). This allows matter in the disc to fall onto the companion star while slowing the orbit contraction, increasing the potential for a stable, long-lived binary system.¹

For some DWD binaries, the mass transfer stream will directly impact the surface of the com-

panion star. In doing so, there is no longer an obvious mechanism to return the orbital angular momentum from the transferred mass to the orbit. The division between the disc accretion and direct impact has been studied before (see Sepinsky et al. 2014; Marsh et al. 2004; Gokhale et al. 2007, and references therein, hereafter Paper I, Marsh2004, and Gokhale2007, respectively).

As in Marsh2004 and Gokhale2007, we showed in Paper I that mass transfer through direct impact can either increase or decrease the semi-major axis of the system, depending on the amount of angular momentum and mass exchanged between the components. If direct impact drives the system apart, both Marsh2004 and Gokhale2007 showed that a stabilizing accretion disc is likely to be created. If direct-impact mass transfer decreases the semi-major axis, the mass transfer rate may eventually become unstable, which can result in a merger. If the total mass of the system is in excess of the Chandrasekhar limit, such merger events could lead to a Type Ia supernova (Woosley and Weaver 1986).

Marsh2004 and Gokhale2007 both calculated of the long term evolution of such systems. Marsh2004 concluded that the population of DWD binaries is likely lower than previously anticipated as a result of the high percentage of systems undergoing direct-impact accretion that become unstable. Gokhale2007 improved upon the analysis of Marsh2004 by permitting the spin of the donor to vary and by including the effects of tidal forces from the donor star (Marsh2004 only examined tidal forces arising from asynchronicity between the accretor and the orbit. In their calculation, the spin of the donor was fixed to that of the orbit throughout so that no tides arose from asynchronicity between the donor and orbit.) The modifications of Gokhale2007 resulted in an increase in the number of stable systems which can be seen in Figures 2 and 3 in section 4. In Paper I we built upon both of these studies, providing direct ballistic integrations of the mass transfer stream (as opposed to the previous method using an approximation adopted from Verbunt and Rappaport (1988)). We showed that removing this approximation which accounts for the complex three-body dynamics of the ejected mass can have a significant impact upon the angular momentum exchange.

¹We note that we have not considered the possibility of the white-dwarf components having some residual, non-degenerate, hydrogen-rich outer layers. In a recent analysis, Shen (2015) showed that the inclusion of such effects and associated nova-like outbursts may predominantly lead to mergers for both direct-impact and disc accretion.

In this paper, we apply the results of Paper I to determine the long-term evolution of double white dwarf binaries in a fully self-consistent manner. In section 2, we introduce the equations which govern the long-term evolution of DWD systems and discuss the differences between this method and the method utilized by previous studies. In section 3 we discuss some details of our long-term numerical integrations. In section 4 we discuss the results of our solutions and analyze the results in comparison to those of previous works. We conclude in section 5.

2. Equations of Long-term Evolution

2.1. Basic Assumptions

Following Paper I, we consider a close binary system of two white dwarfs with masses M_A and M_D , volume-equivalent radii of R_A and R_D , and uniform rotation rates Ω_A and Ω_D with axes perpendicular to the orbital plane for the accretor and donor, respectively.² We assume the mass of each star is distributed spherically symmetrically. As in the analyses of Marsh2004 and Gokhale2007, we assume the binary to remain in a circular Keplerian orbit throughout its evolution. The radius of each object is assigned following Eggleton’s zero-temperature mass-radius relation (equation 15 of Verbunt and Rappaport (1988)). We assume that both the donor and accretor initially rotate synchronously with the orbit (Marsh2004, Gokhale2007).³ We choose the initial semi-major axis of the orbit such that the volume-equivalent radius of the donor (R_D) is equal to the volume-equivalent radius of its Roche lobe as fit by Eggleton (1983).

²Throughout this paper, the subscripts “A” and “D” will correspond to the accretor and donor, respectively.

³We note that there may exist a substantial population of DWD with non-zero eccentricity and asynchronous components prior to the onset of direct impact accretion (Willems et al. (2007); Bours et al. (2014) and references therein). For this analysis, we limit our scope to systems that are initially circular. Initially circular systems are expected to remain circular due to tidal circularization. A more thorough treatment of the initial parameter-space including eccentricity and asynchronicity will be presented in a forthcoming paper.

2.2. Evolution of angular momentum

As described in Marsh2004 and Gokhale2007, the orbital evolution of a circular binary system can be described by its orbital angular momentum. We begin by presenting each of the components that can lead to a change in the orbital angular momentum.

The total angular momentum, J_{tot} , of a binary system is given by the sum of the orbital angular momentum, J_{orb} , and the spin angular momenta, $J_{spin,A}$ and $J_{spin,D}$, of the accretor and donor, respectively:

$$J_{tot} = J_{orb} + J_{spin,A} + J_{spin,D}. \quad (1)$$

The orbital angular momentum is given by

$$J_{orb} = \sqrt{\frac{Ga}{M}} M_A M_D \quad (2)$$

where $M = M_A + M_D$, G is the gravitational constant, and a is the semi-major axis of the system. The spin angular momenta of the accretor and donor are $J_{spin,A} = k_A M_A R_A^2 \Omega_A$ and $J_{spin,D} = k_D M_D R_D^2 \Omega_D$, respectively, where k_A and k_D are dimensionless constants depending upon the internal structure of the accretor and donor, respectively. It follows that:

$$J_{tot} = \sqrt{\frac{Ga}{M}} M_A M_D + k_A M_A R_A^2 \Omega_A + k_D M_D R_D^2 \Omega_D. \quad (3)$$

There are three effects that change the orbital angular momentum over time: mass transfer (MT), tides, and gravitational radiation (GR). Assuming each effect is independent of the others, we can then write the total change of the orbital angular momentum as the sum of the changes due to each of the above effects, with subscripts, as noted above, for each of the respective components:

$$\dot{J}_{orb} = \dot{J}_{orb,MT} + \dot{J}_{orb,tides} + \dot{J}_{orb,GR}. \quad (4)$$

To determine the total change in the angular momentum, then, we simply need to write the change due to each of the above effects.

The change in orbital angular momentum due to GR for a circular orbit is given by:

$$\dot{J}_{orb,GR} = -\frac{32}{5} \frac{G^3}{c^5} \frac{M_A M_D M}{a^4} J_{orb} \quad (5)$$

(see for example, Landau and Lifshitz 1975).

Prior to the onset of mass transfer, the semi-major axis of the binary will have been shrinking due to the effects of GR as seen in equation (5). During this time, tidal coupling will act to circularize the binary as well as synchronize the spins of the stars with the orbit. At the onset of mass transfer, we assume the spins and orbit to be synchronized. As mass transfer begins, angular momentum will be exchanged between the spins of the component stars and the orbit (see Paper I). Any resulting asynchronization between the spins and the orbit leads to tidal coupling, the strength of which will determine how much of the spin angular momentum of the accretor is returned to the orbit. This will ultimately affect the stability of the mass transfer process.

As in Gokhale2007, we model the change in the binary orbital angular momentum due to tides by:

$$\dot{J}_{orb,tides} = \frac{k_A M_A R_A^2}{\tau_A} \omega_A + \frac{k_D M_D R_D^2}{\tau_D} \omega_D. \quad (6)$$

The first term on the right-hand side of this equation represents the torque due to dissipative coupling upon the accretor, and the second term the torque upon the donor. These torques are parameterized in terms of the synchronization time-scales of the accretor, τ_A , and donor, τ_D and are linearly proportional to the difference between the component and orbit spin,

$\omega_{\Omega_i} = \Omega_i - \Omega_{orb}$, with $i \in \{A, D\}$ for the accretor and donor, respectively. Here, Ω_{orb} is the angular velocity of the circular orbit:

$$\Omega_{orb} = \sqrt{\frac{GM}{a^3}} \quad (7)$$

and $k_i M_i R_i^2$ are the moments of inertia of each component, with k_i being the inertial constant.

The values of τ_A and τ_D determine the strength of tidal coupling relative to MT and GR. As in Gokhale2007, we examine both the cases of $\tau_A = \tau_D = 10^{15}$ years (weak tidal coupling) and $\tau_A = \tau_D = 10$ years (strong tidal coupling). The tidal-synchronization timescales are discussed further in 2.7.

To determine $\dot{J}_{orb,MT}$, we follow Paper I, which uses the ballistic mass transfer calculations of Sepinsky et al. (2010) to determine the instantaneous effect of mass transfer on DWD systems.

This method uses a fully self-consistent, conservative, ballistic model of the transferred mass to determine the orbital parameters of the system after a single mass-transfer event. As seen in that paper, provided the mass transferred is small compared to the total mass of the binary system, the change in the orbital parameters per unit mass that results is directly proportional to the mass transfer rate:

$$\dot{J}_{orb,MT} = \frac{\Delta J_{orb,b}}{M_P} \dot{M}_D \quad (8)$$

where $\Delta J_{orb,b}$ is the change in the orbital angular momentum for the DWD as calculated by the above ballistic model for a single mass transfer event ejecting a particle of mass M_P . In this method, changes in $J_{orb,MT}$ (and changes in all orbital parameters) are calculated at each time-step by integrating the three-body system consisting of the two stars and the discrete particle representing the mass transfer stream. The change in the $J_{orb,MT}$ per unit mass transferred is independent of the mass of the ejected particle as long as $M_P \ll M_D, M_A$. For the calculations here, we use $M_P = 10^{-8} M_\odot$. The rate of change of $J_{orb,MT}$ is then determined by multiplying by the current mass-transfer rate of our evolving DWD, \dot{M}_D . The calculation of \dot{M}_D will be discussed in section 2.5.

2.3. Differential equations for long-term evolution

Using the above rates of change for the orbital angular momentum, we are now ready to develop the equations for long-term evolution. It follows from equation (2) that

$$\frac{\dot{J}_{orb}}{J_{orb}} = (1 - q) \frac{\dot{M}_D}{M_D} + \frac{1}{2} \frac{\dot{a}}{a} \quad (9)$$

for conservative mass transfer ($\dot{M} = 0$).⁴ We let $q = M_D/M_A$.

2.3.1. Evolution of the semi-major axis

As in section 2.2 for the orbital angular momentum, we examine the changes of the semi-major axis due to mass transfer, tides, and GR. We assume that each effect is independent, and write the

⁴Recall that we assume the orbit remains circular throughout.

total change in the semi-major axis due to each of the above effects, respectively, as:

$$\dot{a} = \dot{a}_{MT} + \dot{a}_{tides} + \dot{a}_{GR}. \quad (10)$$

To calculate \dot{a}_{MT} , we utilize the model for mass transfer developed in Sepinsky et al. (2010). The differences between this model and models used in other analyses will be discussed in the section 2.4. Using this method, we calculate the time rate of change of a due to mass transfer as

$$\dot{a}_{MT} = \frac{\Delta a_b}{M_P} \dot{M}_D. \quad (11)$$

Here, Δa_b is the change in the semi-major axis for the DWD as calculated by the above ballistic model of Sepinsky et al. (2010) as described in section 2.2 for the orbital angular momentum.

Next we calculate \dot{a}_{tides} and \dot{a}_{GR} . We cannot use the standard tidal prescription for changes in the semi-major axis following Hut (1981) because, following Marsh2004 and Gokhale2007, we used a different metric for changing the spin angular momentum due to tides (equation [6]). Instead, we must develop \dot{a}_{tides} from that angular momentum change. Holding the donor mass constant ($\dot{M}_D = 0$) for the final two terms of equation (10) we can combine equation (4) with equation (9) to obtain:

$$\frac{\dot{J}_{orb,tides}}{J_{orb}} + \frac{\dot{J}_{orb,GR}}{J_{orb}} = \frac{1}{2a} \dot{a}_{tides,GR} \quad (12)$$

where $\dot{a}_{tides,GR}$ is the total change of the semi-major axis due to the combined effects of tides and GR. Assuming as before that changes to the semi-major axis due to tides and changes due to GR are independent we can re-write the above as:

$$\frac{\dot{J}_{orb,tides}}{J_{orb}} + \frac{\dot{J}_{orb,GR}}{J_{orb}} = \frac{1}{2a} \dot{a}_{tides} + \frac{1}{2a} \dot{a}_{GR}. \quad (13)$$

Using equations (2), (5), and (6), it follows that:

$$\begin{aligned} \dot{a}_{tides} &= 2a \frac{1}{M_A M_D} \sqrt{\frac{M}{G a}} \\ &\times \left(\frac{k_A M_A R_A^2}{\tau_A} \omega_A + \frac{k_D M_D R_D^2}{\tau_D} \omega_D \right) \end{aligned} \quad (14)$$

and

$$\dot{a}_{GR} = -\frac{64}{5} \frac{G^3}{c^5} \frac{M_A M_D M}{a^3} \quad (15)$$

For our purposes, we rewrite the two tidal components in terms of the rotation rates of the accretor and the donor relative to the orbital angular velocity, which we define as f_A and f_D , respectively. The rotation rates can be written in terms of the rotational angular velocities of the stars, Ω_i and the angular velocity of the circular orbit, Ω_{orb} :

$$f_i - 1 = \frac{\Omega_i - \Omega_{orb}}{\Omega_{orb}} = \frac{\omega_i}{\Omega_{orb}} \quad (16)$$

Using equations (7) and (16), we can rewrite equation (14) as

$$\dot{a}_{tides} = \frac{2M}{a M_A M_D} (\alpha_A + \alpha_D) \quad (17)$$

where

$$\alpha_A = \frac{k_A M_A R_A^2}{\tau_A} (f_A - 1) \quad (18)$$

and

$$\alpha_D = \frac{k_D M_D R_D^2}{\tau_D} (f_D - 1). \quad (19)$$

Finally, we can insert equations (11), (15), and (17) into equation (10) to obtain the equation for the evolution of the semi-major axis with time:

$$\begin{aligned} \dot{a} &= \frac{\Delta a_b}{M_P} \dot{M}_D + \frac{2M}{a M_A M_D} (\alpha_A + \alpha_D) \\ &\quad - \frac{64}{5} \frac{G^3}{c^5} \frac{M_A M_D M}{a^3}. \end{aligned} \quad (20)$$

2.3.2. Evolution of the component rotation rates

Next, we find the equations for the evolution of the component spins, f_A and f_D . Like the changes to the semi-major axis (equation [10]), the changes in f_A and f_D can be separated into three components:

$$\dot{f}_i = \dot{f}_{i,MT} + \dot{f}_{i,tides} + \dot{f}_{i,GR} \quad (21)$$

with $i \in \{A, D\}$.

Analogous to \dot{a}_{MT} in equation (11), the change in f_i due to mass transfer, $\dot{f}_{i,MT}$ can be written as:

$$\dot{f}_{i,MT} = \frac{\Delta f_{b,i}}{M_P} \dot{M}_D. \quad (22)$$

Here $\Delta f_{b,i}$ is the change in the rotation rates of star i resulting from a single mass transfer event in the formulation of Sepinsky et al. (2010) as described in section 2.2.

As in equation (3), the spin angular momentum of each component can be written as

$$J_{spin,i} = k_i M_i R_i^2 f_i \Omega_{orb}. \quad (23)$$

where we have substituted f_i from equation (16).

Since we have already determined the change in f_i due to mass transfer (equation [22]), we can determine $\dot{f}_{i,tides}$ and $\dot{f}_{i,GR}$ by differentiating equation (23) with the mass held constant:

$$\begin{aligned} \dot{J}_{spin,i} \Big|_{M_i} &= k_i M_i R_i^2 \Omega_{orb} (\dot{f}_{i,tides} + \dot{f}_{i,GR}) \\ &- \frac{3}{2} k_i M_i R_i^2 \Omega_{orb} f_i \frac{1}{a} (\dot{a}_{tides} + \dot{a}_{GR}) \end{aligned} \quad (24)$$

where the second term arises due to the dependence of Ω_{orb} on the semi-major axis (equation [7]). We note that, because we are holding the mass constant, the second term depends only upon changes due to tides and GR, and not changes due to mass transfer. Changes to f_i due to the effect of mass transfer on the semi-major axis are fully accounted for by equation (22).

Since we do not include any GR effects on the spin angular momentum of the components, conservation of angular momentum dictates that any changes in the spin angular momentum of a component must be equal and opposite to the changes in the orbital angular momentum of the system due to tides acting on that component. Combining equations (6), (7), and (16), we have:

$$\dot{J}_{spin,i} \Big|_{M_i} = -\frac{k_i M_i R_i^2}{\tau_i} \Omega_{orb} (f_i - 1). \quad (25)$$

By combining equations (24) and (25) and rearranging, we can write $\dot{f}_{GR,i} + \dot{f}_{tides,i}$ as:

$$\begin{aligned} \dot{f}_{GR,i} + \dot{f}_{tides,i} &= -\frac{(f_i - 1)}{\tau_i} + \\ &\frac{3}{2} \frac{f_i}{a} \left[-\beta + \frac{2}{a} \frac{M}{M_A M_D} (\alpha_A + \alpha_D) \right] \end{aligned} \quad (26)$$

where we have used equations (15), (17)–(19), and let:

$$\beta = \frac{64}{5} \frac{G^3}{c^5} \frac{M_A M_D M}{a^3}. \quad (27)$$

Following the form of equation (21), we can combine equations (22) and (26) to write the equa-

tions for the evolution of f_A and f_D :

$$\begin{aligned} \dot{f}_A &= \frac{\Delta f_{b,A}}{M_P} \dot{M}_D - \frac{f_A - 1}{\tau_A} + \\ &\frac{3}{2} \frac{f_A}{a} \left[-\beta + \frac{2}{a} \frac{M}{M_A M_D} (\alpha_A + \alpha_D) \right] \end{aligned} \quad (28)$$

$$\begin{aligned} \dot{f}_D &= \frac{\Delta f_{b,D}}{M_P} \dot{M}_D - \frac{f_D - 1}{\tau_D} + \\ &\frac{3}{2} \frac{f_D}{a} \left[-\beta + \frac{2}{a} \frac{M}{M_A M_D} (\alpha_A + \alpha_D) \right]. \end{aligned} \quad (29)$$

2.3.3. Evolution of the eccentricity

We assume that the eccentricity of these systems is zero prior to the onset of direct-impact accretion. During the three-body integration of a single mass-transfer event, it is possible for the binary to develop a small eccentricity. However, for simplicity and in accordance with Marsh2004 and Gokhale2007, we force the eccentricity to remain zero throughout. Because the system begins in a circular orbit, and due to the action of tidal forces and gravitational wave emission which both act to circularize the orbit, it is unlikely for any significant eccentricity to develop. In order to keep this orbital angular momentum in the orbit, we manually set our new semi-major axis to:

$$a = a_I (1 - e^2) \quad (30)$$

where e is the eccentricity gained by the system during mass transfer and a_I is the semi-major axis of the eccentric orbit. Using this modification, we force:

$$\dot{e} = 0, \quad (31)$$

and still conserve orbital angular momentum. A more thorough analysis in which we allow eccentricity to vary throughout the entire calculation will be presented in a forthcoming paper.

2.3.4. Mass transfer rates

Finally, the changes in the masses of the accretor and donor are given, respectively, by:

$$\frac{dM_A}{dt} = -\dot{M}_D \quad (32)$$

$$\frac{dM_D}{dt} = \dot{M}_D \quad (33)$$

The mass loss rate of the donor, \dot{M}_D is obtained as described in section 2.5.

Together, the set of equations (20), (28), (29), (31), (32), (33) can be integrated in time to calculate the evolution of the system.

2.4. Differences from previous analyses

There are several differences between our treatment of mass transfer and those of Marsh2004 and Gokhale2007. In order to calculate the angular momentum exchange during mass transfer, the studies of Marsh2004 and Gokhale2007 both utilize a numerical prescription based on Verbunt and Rappaport (1988). In that formulation, it is assumed that the angular momentum transferred from the orbit to the spin of the accretor is exactly equal to the angular momentum of the ballistic particle in a circular orbit around the donor at its average radius during its motion from donor to accretor. Where the analysis of Marsh2004 keeps the spin of the donor fixed, Gokhale2007 does allow the spin of the donor to vary, and notes that in doing so, the number of stable systems increases. However, the allowance of variation in donor spin is not done self-consistently. By introducing the spin angular momentum of the donor, there are now three separate sources/sinks of angular momentum: the spin of the donor, the spin of the accretor, and the orbit. Paper I showed that angular momentum is transferred between each during mass transfer, and that the fraction of angular momentum transferred between each is strongly dependent on the ballistic trajectory of the transferred mass, and hence the system properties. In this paper, we apply the ballistic calculations of Paper I to lift the dependence on the Verbunt and Rappaport (1988) approximations to more accurately determine the flow of angular momentum between the component spins and the orbit.

Since orbital angular momentum changes are directly linked to changes in the mass ratio and semi-major axis, much can be learned from analyses such as that of Gokhale2007 and Marsh2004. However, a more complete analysis demands a thorough consideration of the spin angular momenta of the stars as well due to their indirect effect upon the system properties through tidal coupling. This is accomplished via the ballistic calculations described above, which evaluate the

three-body problem throughout the evolution of the system to determine the precise effect mass transfer has on the evolution of the system. These calculations take into account not only the immediate feedback on the orbit and spin of the accretor during ejection, but also (1) the gravitational effect on the orbit during the mass transfer process, (2) a calculation of the precise moment when the particle impacts the surface of the accretor, (3) the instantaneous properties of both the accretor and particle at impact, including the angle of impact, and (4) correctly divides the momentum of the impacting particle between linear and angular momentum based upon the angle of impact and the rotation rate of the accretor. We can then examine the angular momentum exchange between all components, the spins of both stars and the orbit, and do so in a way that allows the spins of both stars to vary self-consistently.

2.5. Calculation of mass-transfer rate

As in Marsh2004, we define the overflow of the Roche lobe as:

$$\Delta = R_D - R_L \quad (34)$$

where R_D is the radius of the donor and R_L is the radius of the donor's Roche lobe. The way in which the mass-transfer rate varies with Δ has been investigated in many analyses (see, for example, Paczynski and Sienkiewicz (1972); Webbink (1977); Savonije (1978)). In accordance with Marsh2004, we approximate the mass transfer as adiabatic (Webbink 1984). In the adiabatic regime the mass transfer rate is given by:

$$\dot{M}_D = \frac{8\pi^3}{9} \left(\frac{5Gm_e}{h^2} \right)^{3/2} (\mu_e m_n)^{5/2} \times \frac{1}{P_{orb}} \left(\frac{3\mu M_D}{5r_L R_2} \right)^{3/2} \frac{1}{\sqrt{a_2(a_2 - 1)}} \Delta^3 \quad (35)$$

for $\Delta > 0$ and zero for $\Delta < 0$ (using results from Webbink (1984); Chandrasekhar (1967); Webbink (1977)). Here, m_e is the mass of an electron, m_n is the mass of a nucleon, μ_e is the mean number of nucleons per free electron in the outer layers of the donor (assumed here to be two), P_{orb} is the orbital period, $r_L = R_L/a$, and μ and a_2 are given by the following:

$$\mu = \frac{M_D}{M_A + M_D} \quad (36)$$

$$a_2 = \frac{\mu}{x_{L1}^3} + \frac{1 - \mu}{(1 - x_{L1})^3} \quad (37)$$

where x_{L1} is the distance from the center of the donor to the inner Lagrangian point of the donor, in units of the semi-major axis (Webbink 1977).

2.6. Calculation of Roche lobe

In the case of Marsh2004, where the rotational velocity of the donor is fixed to the orbital velocity and where the orbit is circular throughout, the shape and volume of the Roche lobe depends only upon the mass ratio of the system. In that case, the approximation from Eggleton (1983),

$$R_{L,\text{Egg}} = a \frac{0.49q^{2/3}}{0.6q^{2/3} + \ln(1 + q^{1/3})}, \quad (38)$$

is sufficient. However, for eccentric and/or non-synchronous binaries, the shape and volume of the roche lobe also depend upon the eccentricity, the true anomaly, ν , and the rotation rate, which can be expressed by the parameter:

$$\mathcal{A}_i(e, f, \nu) = \frac{f_i^2(1 + e)^4}{(1 + e \cos \nu)^3} \quad (39)$$

see Sepinsky et al. (2007). Other analyses have considered the dependence of the Roche lobe on asynchronicity. In the case of a circular orbit, the Roche lobes described in Sepinsky et al. (2007) using the Roche-lobe parameter \mathcal{A}_i directly reflect the equipotential surfaces described in Plavec (1958) and Kruszewski (1963). We note that this asynchronicity parameter \mathcal{A}_i depends on the rotation rate of the component star in question, which means the size of the Roche lobe can be different for each object in the system.

For our calculations, we perform a Monte Carlo integration to calculate the volume-equivalent Roche lobe radius (as outlined in Sepinsky et al. (2007)) over a two-dimensional grid in \mathcal{A} - q parameter-space. We then use a bilinear interpolation function to create a continuous function for the Roche lobe from the two-dimensional grid. The interpolated function is accurate to 0.01 percent or better in comparison to the Monte Carlo integration at equivalent points.

In section 4.4, we examine the dependence of the results on the size of the Roche lobe. There, we compare the evolution of the DWD systems using

the Eggleton function for the roche lobe, $R_{L,\text{Egg}}$, to the evolution including the asynchronicity parameter which we name $R_{L,\text{asynch}}$.

2.7. Synchronization time-scale

As the spin angular momentum of the accretor increases due to impact from the mass transfer stream, tidal coupling will redistribute some of this angular momentum back into the orbit. The strength of this tidal coupling is dependent upon the synchronization time-scales, τ_A and τ_D , as seen in equation (6). Campbell (1984) calculated this timescale as:

$$\tau_C = 1.3 \times 10^7 \left(\frac{M_A}{M_D} \right)^2 \left(\frac{a}{R_A} \right)^6 \left[\frac{M_A/M_\odot}{L_A/L_\odot} \right]^{5/7} \text{ yr} \quad (40)$$

Following Marsh2004, we retain the scaling with mass ratio and orbital separation, but, because of the uncertainty of the overall magnitude of the time-scale, we allow the magnitude to vary. We define the overall magnitude by the time-scale at the moment of first contact and assume, as in Marsh2004 and Gokhale2007, that

$$\tau_A(t) = C_A \left(\frac{M_A}{M_D} \right)^2 \left(\frac{a}{R_A} \right)^6 \quad (41)$$

and

$$\tau_D(t) = C_D \left(\frac{M_D}{M_A} \right)^2 \left(\frac{a}{R_D} \right)^6. \quad (42)$$

where C_A and C_D are constants defined such that $\tau_A(0) = \tau_{A,I}$ and $\tau_D(0) = \tau_{D,I}$. Here, $\tau_{A,I}$ and $\tau_{D,I}$ are the initial synchronization time-scales. As in Gokhale2007, we explore two different values for the synchronization time-scale at contact: 10^{15} years (very weak tidal coupling) and 10 years (very strong tidal coupling). Much work on tidal synchronization in DWDs has been done (see, for example, Valsecchi et al. (2013); Fuller and Lai (2014); Burkart, Quataert, and Arras (2014)). These analyses have shown that shorter synchronization time-scales may be a better approximation for systems with short orbital periods, as we consider in this analysis, which may lend credence to our 10 year synchronization time-scale. For simplicity, we use the same initial time-scale for the donor and accretor ($\tau_{A,I} = \tau_{D,I}$) and refer to the initial synchronization time-scale for both stars as simply τ .

We have now determined the set of differential equations which governs the evolution of the DWDs undergoing direct-impact accretion, including the methods for calculating the Roche lobe size, the mass transfer rate, and the synchronization timescales which determine the strength of tidal coupling. We now have all the steps in place to solve for the long-term evolution of the systems.

3. Numerical Solutions

We integrate equations (20), (28), (29), (31), (32), (33) using an 8th order Runge Kutta ordinary differential equation solver (Galassi et al. 2006). Excluding the losses due to gravitational radiation, the total energy and momentum of the system are conserved throughout the integration over the entire parameter space to one part in 10^{-3} or better. At the end of the evolution, we calculate $J_{conserve} = J_{total} - J_{total,I} + J_{total,GR}$ where $J_{total,I}$ is the initial total angular momentum and $J_{total,GR}$ is the total angular momentum lost to gravitational radiation. If angular momentum is perfectly conserved, we expect $J_{conserve}$ to be equal to zero.

Figure 1 shows the final value of $J_{conserve}$ for both synchronization time-scales at contact over the entire parameter space of interest for solutions calculated using both the Eggleton approximation (left), $R_{L,Egg}$, and $R_{L,asynch}$ (right) for the calculation of the Roche lobe. The colors correspond to different values of $J_{conserve}$ as described in the caption. In general, systems with a smaller total mass conserve total angular momentum better than systems with a higher mass. For many of the systems in the lower right, this is due to the fact that they reach a stable configuration (disc accretion) early in the integration. Therefore, the integration needs to run for only a few orbits. Systems where $J_{conserve}$ is larger tend to be systems where the numerical integration runs for many orbits, allowing systematic errors in the numerical integration to accumulate. Even so, all systems presented in this paper conserve total angular momentum to better than 1% throughout the entire evolution.

We integrate over a period of 1 Gyr. As in Marsh2004, if \dot{M}_D exceeds $0.01 M_{\odot}/\text{yr}$ at any point during the integration, the integration stops

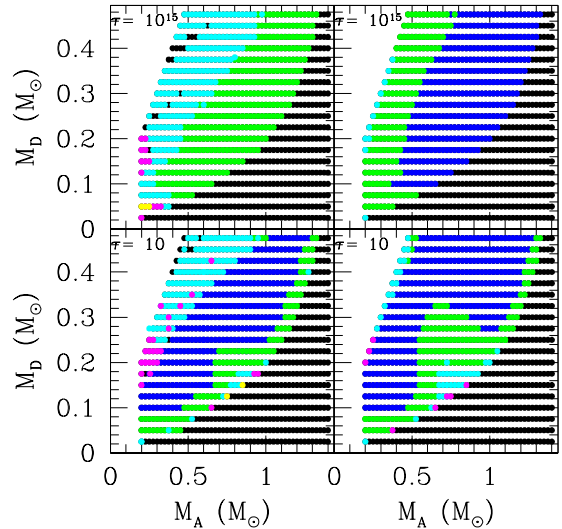


Fig. 1.— Angular momentum conservation over entire parameter space for the two synchronization time-scales. The left-hand panels show the solutions obtained using $R_{L,Egg}$ for the calculation of the Roche lobe and the right-hand panel shows the solutions using $R_{L,asynch}$. Calculated here is $J_{conserve} = J_{total} - J_{total,I} + J_{total,GR}$ at the end of the integration. Blue systems conserve angular momentum to an order of 10^{-3} ; green systems to an order of 10^{-4} ; cyan systems to an order of 10^{-5} ; magenta systems to an order of 10^{-6} ; yellow systems to an order of 10^{-7} ; and black systems to an order of 10^{-8} or better.

and the system is discarded as unstable.

As a system evolves, it is possible to pass back and forth through phases of mass transfer and phases of no mass transfer as the semi-major axis and the two masses change. If the semi-major axis increases enough for mass transfer to stop altogether, the integration proceeds (with $\dot{M}_D = 0$) until the action of gravitational radiation shrinks the orbit sufficiently for mass transfer to resume.

As in Paper I, in this work we are only interested in direct-impact mass transfer where the particle impacts the surface of the accretor within one orbital period. In this case, the evolution of the orbital parameters is determined by the differential equations presented in section 2. If the particle does not accrete within one orbital period, it is likely that the accretion stream will eventually intersect with itself, ultimately leading to the formation of an accretion disc (Sepinsky et al. 2010).

Compared to direct-impact accretion, disc accretion is known to provide a much more efficient

mechanism for redistributing spin angular momentum in the accretor back into the orbit through tidal coupling (Frank, King and Raine 2002). As a result, it is likely that once a system enters a phase of disc accretion it will remain in this phase or perhaps even become detached as the orbital separation continues to grow and the mass ratio decreases due to continued mass transfer. If at any point during our numerical integrations a disc is formed under these circumstances, the integration stops and the system is assumed to be stable throughout its lifetime. A more thorough analysis which continues to track the evolution through potential disc phases will be performed in a future paper. This issue is discussed further in section 4.

3.1. Maximum spin-rate of the accretor

For weak tidal coupling, it is possible for the accretor to be spun up to its breakup rate ($\Omega_k = \sqrt{GM_A/R_A^3}$). We track Ω_A throughout our calculations and note that only one system ever reaches this maximum spin for the accretor. This system, which has an initial donor mass of $0.1 M_\odot$ and an initial accretor mass of $0.275 M_\odot$, is marked by a yellow dot in Figure 2. The accretor spin-rates in all other systems stay below the breakup rate throughout their evolution.

3.2. Super-Eddington accretion

As noted by Marsh2004, there are likely ranges of parameter space where systems, despite being stable, experience super-Eddington accretion at some point during their evolution. It is expected that a possible ultimate consequence of sustained super-Eddington accretion is a merger (Han and Webbink 1999; ?; Marsh et al. 2004), the same result as a dynamically unstable system, as they eventually can reach very high mass-transfer rates.

As in Marsh2004, we calculate the Eddington accretion rate using a modified form of the calculation used by Han and Webbink (1999):

$$\dot{M}_{Edd} = \frac{8\pi G m_p c M_A}{\sigma_T (\phi_{L1} - \phi_a - \frac{1}{2} \mathbf{v}_i^2 + \frac{1}{2} (\mathbf{v}_i - \mathbf{v}_\omega)^2)} \quad (43)$$

where σ_T is the Thomson cross-section of the electron, m_p is the mass of a proton, \mathbf{v}_i is the impact velocity of the accreted particle, and \mathbf{v}_ω is the spin-velocity of the accretor's surface at the

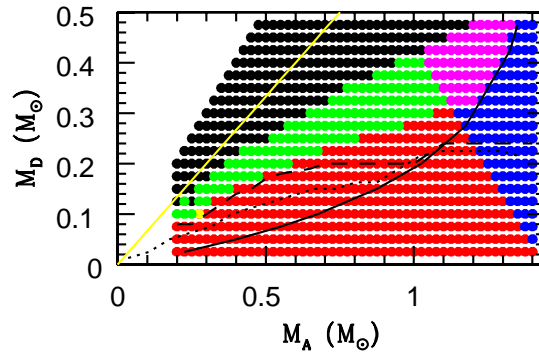


Fig. 2.— Results of evolution with initial tidal synchronization time-scale of $\tau = 10^{15}$ years using the Eggleton approximation for the Roche lobe. Red systems are stable throughout their entire evolution and have a total system mass which is sub-Chandrasekhar ($< 1.44 M_\odot$). Green systems have a total mass which is sub-Chandrasekhar but went through a phase of super-Eddington accretion at some point during the evolution. Blue systems are stable throughout and have a total system mass which is super-Chandrasekhar. Magenta systems have a total mass that is super-Chandrasekhar and undergo a period of super-Eddington accretion. Black systems are unstable, meaning the mass-transfer rate exceeded $0.01 M_\odot/\text{yr}$. The solid yellow line illustrates the widely-used $q > 2/3$ instability boundary (see, for example, Marsh2004). The solid black line shows the boundary between disc and direct-impact accretion for initially synchronous and circular binaries. The dotted black line and dashed black line illustrate the boundary between stable systems and super-Eddington systems for the $\tau = 10^{15}$ year timescale in Marsh2004 and Gokhale2007, respectively (see Figure 5 in Marsh2004 and Figure 7 in Gokhale2007).

point of impact, both measured in the co-rotating frame of reference.

In the Marsh2004 analysis, a set of impact velocities and locations were pre-computed and were interpolated during the calculations to calculate \mathbf{v}_i and \mathbf{v}_ω . Instead we are able to calculate \mathbf{v}_i and \mathbf{v}_ω explicitly as part of the three-body integration of the mass transfer event. We track the mass-transfer and flag systems that eventually exceed the maximum mass-transfer as unstable.

4. Results

Using the techniques described above, we computed evolution over a grid in M_A, M_D parameter space to determine the long-term stability of various systems. The grid was computed for two different tidal synchronization time-scales at contact:

10^{15} years and 10 years.

4.1. Evolution of systems using Eggleton Roche lobe

We first present the results of our numerical integrations using the standard Eggleton approximation for the calculation of the Roche lobe (equation [38]), which does not take into account asynchronicity between the donor and orbit. The Eggleton approximation was used in the analyses of both Marsh2004 and Gokhale2007.

Figure 2 shows the end result of systems with an initial synchronization time-scale of $\tau = 10^{15}$ years using $R_{L,Egg}$. As mentioned in section 3, we assume that once a disc is reached, the system will remain stable for the remainder of its evolution, therefore we stop the integration once a disc is formed. With the exception of the unstable black systems (whose evolution stops when the mass transfer rate exceeds the maximum limit of $0.01 M_{\odot}/\text{yr}$), the evolution of all systems in this plot is stopped when the system reaches a phase of disc accretion. The time it takes to reach this phase of disc accretion varies from system to system.

The solid black line in Figure 2 shows the boundary between disc and direct-impact accretion for initially synchronous and circular binaries. All systems to the right of and below this line begin evolution in a disc phase. Therefore, these systems are assumed stable from the onset of evolution and do not evolve past $t = 0$. Since these systems do not evolve in time, the angular momentum is perfectly conserved, as shown by

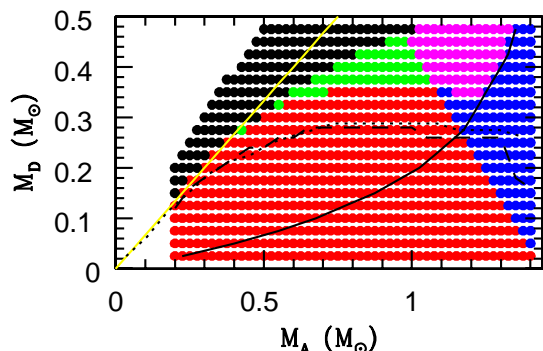


Fig. 3.— As Figure 2, but with $\tau = 10$ years.

the black systems in the lower right of the plots in Figure 1. All systems to the left of and above this line begin evolution in a direct-impact phase. We will discuss how we handle disc accretion further in section 4.2.

Figure 3, analogous to Figure 2, shows the end results of systems with initial synchronization time-scales of $\tau = 10$ years using $R_{L,Egg}$ for the Roche lobe calculation.

The sub-Chandrasekhar, sub-Eddington systems shown in red in Figures 2 and 3 are expected to remain stable throughout their lifetimes and are therefore characterized as likely AM CVn progenitors. As observed from the dotted and dashed black lines in Figures 2 and 3, the region of parameter space occupied by such systems in Gokhale2007 (dashed line) increased the number of stable systems compared to Marsh2004 (dotted line); our analysis reveals a further increase in the extent of this region of parameter space. This observation holds true for both the 10^{15} year time-scale (Figure 2) and the 10 year time-scale (Figure 3).

Gokhale2007 noted that by allowing the spin of the donor to vary and by including the resulting effects of tidal coupling between the donor’s spin and the orbit, the number of stable systems increased compared to the analysis of Marsh2004 (as observed by comparing the dotted versus dashed lines in both Figures 2 and 3). As described in section 2.4, the main difference between our analysis and that of Gokhale2007 is in the treatment of the way we handle angular momentum evolution during the direct impact accretion process. In observing the increase in the number of stable systems compared to the analysis of Gokhale2007, we conclude that by utilizing a mass transfer treatment that allows the rotation rates of both components to vary and self-consistently accounts for the exchange of angular momentum between the spins of the components and the orbit, we are able to increase the number of stable systems.

Figures 2 and 3, produced using $R_{L,Egg}$ for the Roche lobe calculation, isolate the effect of our different treatment of the mass transfer process has upon the stability of systems in comparison with Marsh2004 and Gokhale2007. We will discuss the differences resulting from using $R_{L,asynch}$ in section 4.4.

Forming a boundary between the stable (red and blue) and unstable (black) systems are the green and magenta systems, which experience super-Eddington accretion at some point during the integration. Unlike the black systems, whose mass transfer exceeds the allowed limit of $0.01M_{\odot}/\text{yr}$ and are therefore categorized as unstable, these green/magenta super-Eddington systems are categorized as stable. However, it is likely that systemic mass loss is needed for a binary to survive phases of super-Eddington accretion. Han and Webbink (1999) argues that such mass loss may lead to a common envelope surrounding the binary, which will ultimately lead to a merger. In this case, systems which experience super-Eddington accretion would be considered unstable systems. The analyses of Marsh2004 and Gokhale2007 both note that super-Eddington systems are expected to be unstable. We make the same assumption but note that a more thorough treatment of the physics governing systems as they pass through any phases of super-Eddington accretion is necessary to state with certainty whether or not such systems are ultimately stable or unstable.

The green super-Eddington systems have a total mass which is sub-Chandrasekhar, and the magenta super-Eddington systems are super-Chandrasekhar. If we assume super-Eddington systems are ultimately unstable, the magenta systems can be categorized as possible Type Ia supernova progenitors.

As the tidal synchronization time-scale is reduced from $\tau = 10^{15}$ years in Figure 2 to $\tau = 10$ years in Figure 3, we see the parameter space occupied by stable systems grows (red). This is to be expected and in agreement with the analyses of Marsh2004 and Gokhale2007. Stronger tidal coupling will allow more spin angular momentum from the accretor to be transferred back into the orbit, which increases the semi-major axis, causing the mass-transfer rate to decrease. This results in an increase the stability of the systems in general.

4.2. Disc accretion

In both Figures 2 and 3 we see a portion of stable, super-Chandrasekhar, sub-Eddington systems (blue) in the top right corners of our plots. In the analyses of both Marsh2004 and Gokhale2007, this portion of parameter space is occupied by super-Eddington systems, which would be magenta cir-

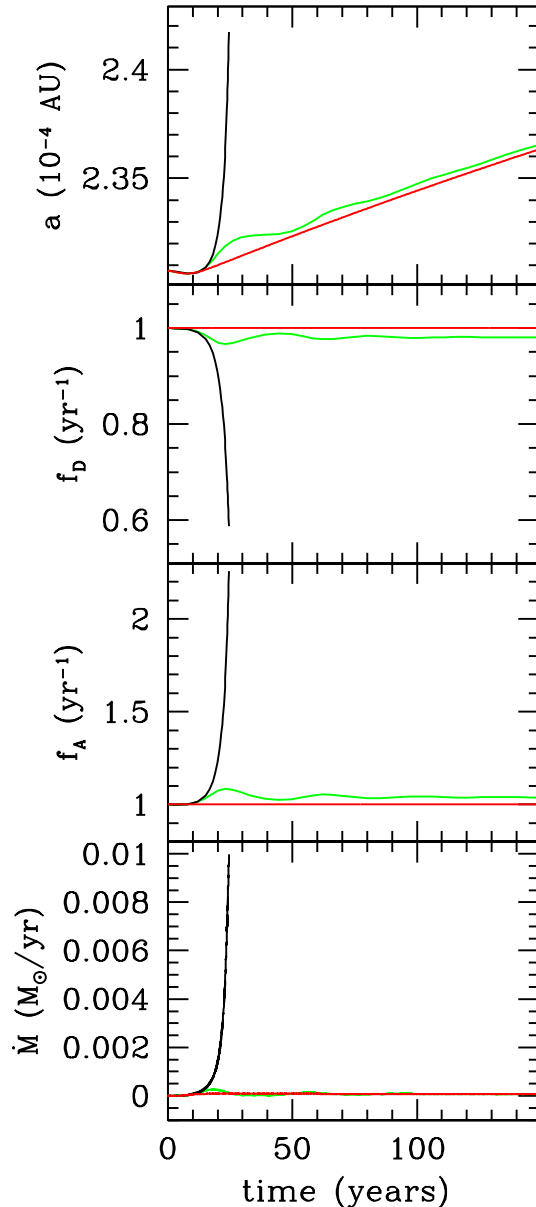


Fig. 4.— Various system properties for the first 150 years of evolution of a system with $M_A = 0.38 M_{\odot}$ and $M_D = 0.8 M_{\odot}$. Evolution using an initial synchronization time-scale of $\tau = 10^{15}$ years is shown in black; this system is unstable (see Figure 3). The same system with $\tau = 10$ years is shown in green; this system is super-Eddington. $\tau = 0.1$ year for this system is shown in red; this system is stable.

cles in our plots. Notice that the dotted and dashed lines of Marsh2004 and Gokhale2007 de-

crease as we move right across the plot, whereas our stability boundary is more extended. This is due to the fact that we do not follow the evolution of the systems past the development of disc accretion, while Marsh2004 and Gokhale2007 both continue to track the evolution of systems through phases of disc accretion.

Here we acknowledge the main limitation of our decision to assume that systems are stable once they reach a phase of disc accretion. The blue systems in the region of parameter space of interest here begin the integration in a disc phase, and are therefore labeled as stable. However, it is feasible that if these high donor-mass systems were allowed to evolve through the initial disc phase, they would eventually become super-Eddington and potentially unstable. In this case, this region of parameter space would more closely conform with the shape of Marsh2004’s and Gokhale2007’s analyses, both of which allow the systems to continue evolving through any phases of disc accretion. As we noted earlier, a more thorough analysis of this region of parameter space which includes treatment of disc accretion will be studied in a forthcoming paper.

4.3. Comparison of system evolution with different tidal time-scales

Figure 4 shows the evolution in time of a system with initial masses of $M_A = 0.8 M_\odot$ and $M_D = 0.38 M_\odot$ for the two different synchronization timescales at contact as well as a third much stronger tidal timescale, $\tau = 0.1$ year, for further illustration. These solutions are obtained using $R_{L,Egg}$ to calculate the Roche lobe. For $\tau = 10^{15}$ years, the system is unstable, for $\tau = 10$ years the system is stable, but passes through a phase of super-Eddington accretion, and for $\tau = 0.1$ year the system is stable and sub-Eddington.

For weak tidal coupling ($\tau = 10^{15}$ years), shown in black, mass transfer causes the rotation rates of the donor and accretor to rapidly decrease and increase, respectively. For the case of stronger tidal coupling ($\tau = 10$ years and $\tau = 0.1$ year; shown in green and red, respectively), tidal forces exist to redistribute angular momentum, working to keep the spins of the donor and accretor synchronous with the orbit ($f_i = 1$).

The rapid increase in the semi-major axis for

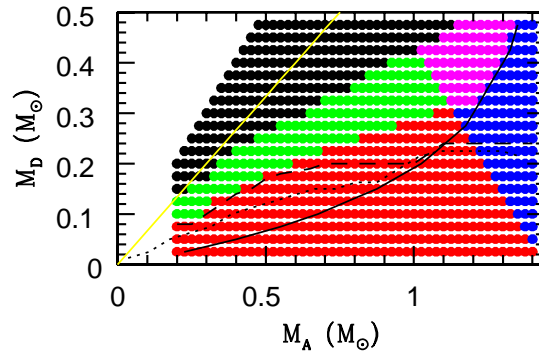


Fig. 5.— As Figure 2, but using $R_{L,asynch}$ for the Roche lobe calculation.

$\tau = 10^{15}$ years is a direct result of the conservation of angular momentum: the angular momentum lost during the spin-down and mass loss of the donor is greater than the angular momentum gained by the accretor. The net decrease in spin angular momentum corresponds to an increase in the orbital angular momentum, increasing the semi-major axis. The mass transfer rate increases rapidly as the mass loss from the donor causes the radius to increase, even as the Roche lobe grows due to the increasing semi-major axis (see equations [34] and [35]).

For the case of strong tidal coupling ($\tau = 10, 0.1$ year) we see a significant decrease in the mass transfer rate, with a correspondingly slower increase in the semi-major axis. The rotation rates of the component white dwarfs remain closer to synchronous, and we do not see the rapid runaway that is evident in the case of weak tidal coupling.

Finally, we note that oscillations in the orbital parameters are seen in the $\tau = 10$ year case, which have been observed before by Gokhale2007. These oscillations are sensitive to small changes in the initial orbital parameters. We discuss this phenomenon further in section 4.5.

4.4. Evolution of systems including the effect of asynchronism on the Roche-lobe size

Here, we show the results of our numerical integrations using $R_{L,asynch}$ to calculate the Roche-lobe size. As discussed in section 2.6, the Eggleton approximation is dependent upon only the mass

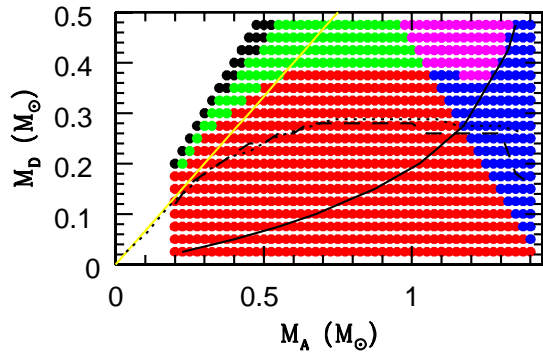


Fig. 6.— As Figure 3, but with $\tau = 10$ years and using $R_{L,asynch}$.

ratio of the binary, whereas $R_{L,asynch}$ accounts for deviations from synchronism.

Figure 5 shows the end results of the systems with initial synchronization time-scales of $\tau = 10^{15}$ years and evolved using $R_{L,asynch}$. The color code remains the same as in Figures 2 and 3 and the dotted and dashed lines from Marsh2004 and Gokhale2007, respectively, for the 10^{15} year time-scale are included for reference. As can be seen, this plot is nearly identical to Figure 2, which was calculated using the Eggleton approximation.

Figure 6 shows the end results of the systems which begin with synchronization time-scales of $\tau = 10$ years. By comparing with Figure 3, we observe that, unlike the 10^{15} year time-scale, $R_{L,asynch}$ has a significant effect upon the end-states of the systems for the 10 year time-scale. In particular, the number of unstable black systems is reduced substantially. The cause of this difference is explained in details below (section 4.5).

In Figure 6, we also observe a slight increase in the number of stable systems across the entire range of accretor masses compared to Figure 3. Additionally, there is a small group of stable red systems beyond the widely-used $q > 2/3$ boundary for instability (for $q > 2/3$, the donor radius will expand faster than the Roche lobe which suggests, simplistically, that such systems will become unstable). However, it is possible for systems with an initial mass ratio higher than $2/3$ to survive, provided that the mass ratio is close to the boundary (see, for example, D’Souza et al. (2006)). Our results, as shown in Figure 6, confirm this obser-

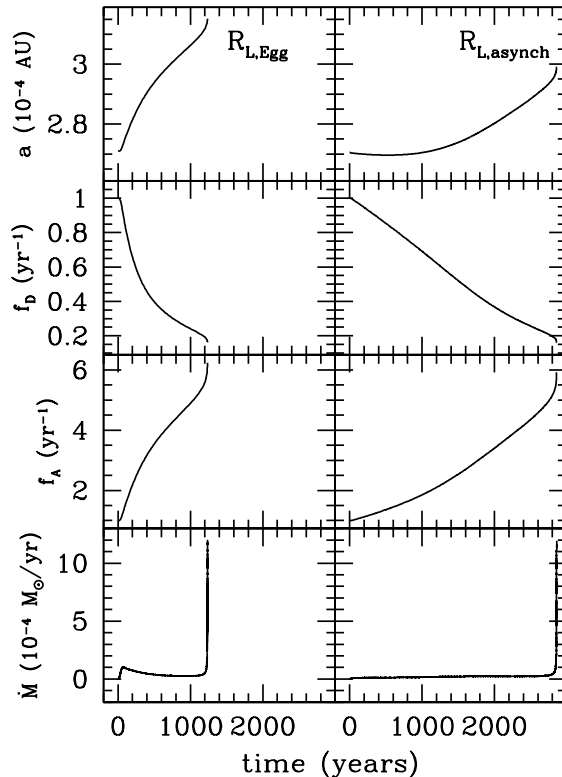


Fig. 7.— Evolution of orbital parameters for $\tau = 10^{15}$ years with initial masses of $M_D = 0.3 M_\odot$ and $M_A = 0.8 M_\odot$. Solutions obtained using the $R_{L,Egg}$ calculation of the Roche lobe on left and the $R_{L,asynch}$ on the right.

vation.

4.4.1. Comparison of the evolution of systems using $R_{L,Egg}$ and $R_{L,asynch}$ solutions for $\tau = 10^{15}$ years

Figure 7 compares the evolution of a system with an initial donor mass of $0.3 M_\odot$ and an initial accretor mass of $0.8 M_\odot$ for $\tau = 10^{15}$ years. On left we show the evolution of various orbital parameters obtained using the Eggleton approximation for the Roche lobe calculation. The right side mirrors the left but shows the evolution using $R_{L,asynch}$ instead of $R_{L,Egg}$. As seen on the plots, the evolution of the orbital parameters happens on a much shorter time-scale for the $R_{L,Egg}$ solution than for the $R_{L,asynch}$ solution. This is due to the fact that, as mass is transferred from the donor to the accretor, the rotation rate of the donor decreases relative to the orbit and the rotation rate

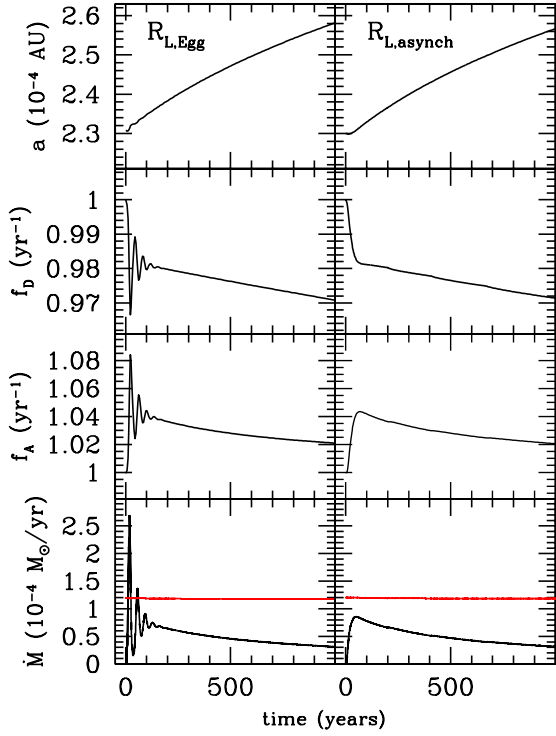


Fig. 8.— Evolution of orbital parameters for $\tau = 10$ years for initial masses, $M_D = 0.38 M_\odot$ and $M_A = 0.8 M_\odot$. First 1000 years of evolution with solutions obtained using $R_{L,Egg}$ for the calculation of the Roche lobe on left and using $R_{L,asynch}$ on right. The red lines show the super-Eddington accretion rate.

of the accretor increases. As the donor spin (f_D) decreases, \mathcal{A} (which is proportional to f_D^2 ; equation 39) also decreases. When using $R_{L,asynch}$, the size of the Roche lobe is inversely proportional to \mathcal{A} . So, as \mathcal{A} decreases, the Roche lobe will increase, which ultimately reduces the mass transfer rate. However, in the $R_{L,Egg}$ calculation, the Roche lobe is insensitive to changes in f_D , so the mass transfer rate is higher relative to that calculated in the solution using $R_{L,asynch}$. Since the mass transfer rate is higher in the Eggleton case, the orbital parameters change more quickly than in the $R_{L,asynch}$ case, as seen in Figure 7.

4.4.2. Comparison of the evolution of systems using $R_{L,Egg}$ and $R_{L,asynch}$ solutions for $\tau = 10$ years

Figure 8 compares the evolution of a system with an initial donor mass of $0.38 M_\odot$ and an ini-

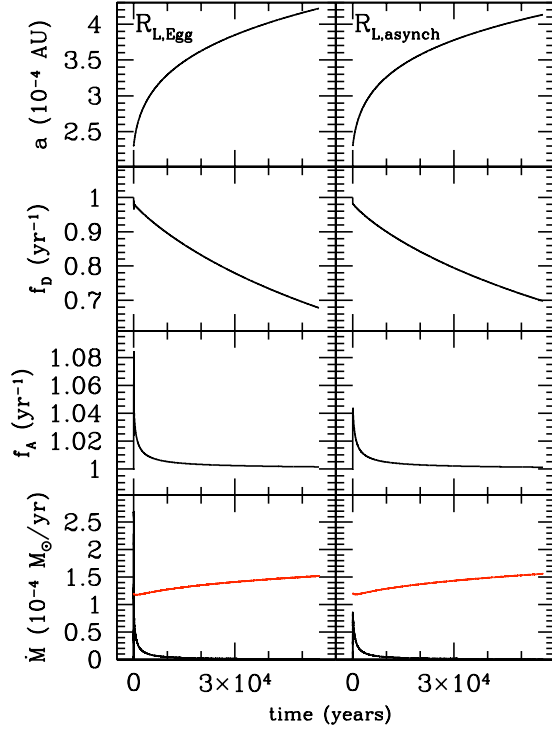


Fig. 9.— Full evolution in time of orbital parameter for $\tau = 10$ years with $M_D = 0.38 M_\odot$ and $M_A = 0.8 M_\odot$. Compare to Figure 8 which shows only the first 1000 years of evolution for this particular system.

tial accretor mass of $0.8 M_\odot$ with $\tau = 10$ years for the first 1000 years of evolution. Figure 9 shows the full evolution of this system, which evolved out to approximately 6×10^4 years before reaching a phase of disc accretion. As in Figure 7, the left panel shows the evolution using $R_{L,Egg}$ and the right panel shows the evolution using $R_{L,asynch}$. As can be seen in Figures 3 and 5, this system is stable under the $R_{L,asynch}$ calculation and super-Eddington under the $R_{L,Egg}$ calculation. Unlike the 10^{15} year time-scale, for the 10 year time-scale, the orbital parameters follow approximately the same path in both the $R_{L,Egg}$ and $R_{L,asynch}$ cases, with the exception being the oscillations seen when using $R_{L,Egg}$. We discuss these oscillations in more detail below.

4.5. Oscillations of orbital parameters

As seen in Figure 8, using $R_{L,asynch}$ to calculate the Roche lobe damps the oscillations observed when using the $R_{L,Egg}$. In both cases, the mass

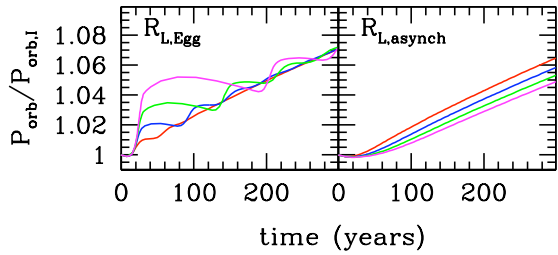


Fig. 10.— Evolution of the orbital period, P_{orb} , compared to its initial orbital period, $P_{orb,I}$, for a system with $M_D = 0.38 M_\odot$ and $M_A = 0.8 M_\odot$ for various synchronization time-scales at contact. Red, blue, and magenta lines represent the orbital periods for synchronization timescales of 20, 30, and 40 years, respectively. The left-hand panel shows the evolution using $R_{L,Egg}$ and the right-hand panel shows the evolution using $R_{L,asynch}$.

transfer rate increases initially, which causes the accretor to spin up and the donor to spin down. In the $R_{L,asynch}$ case, this causes the mass transfer rate to increase at a slower rate relative to the $R_{L,Egg}$ case.⁵ As discussed above, when using $R_{L,Egg}$, the mass transfer rate will continue to increase until tides have transferred sufficient angular momentum from the spin of the components to the orbit to widen the orbit and reduce the mass transfer rate. Once this occurs, the mass transfer rate is reduced and tides continue to redistribute angular momentum between the component spins and the orbit (in this case the donor is spun up while the accretor is spun down). But again, because changes in the donor spin are not accounted for when using $R_{L,Egg}$, the mass transfer rate will again “over shoot” and the oscillations continue. The dependence of the Roche lobe radius upon the donor spin when using $R_{L,asynch}$ slows the changes in the mass transfer rate and damps the oscillations.

Although Figure 8 shows that the short-term evolution of this particular system differs substantially between the $R_{L,Egg}$ and $R_{L,asynch}$ Roche lobe calculations, Figure 9 shows that the long-term evolution of this system is very similar. Although the oscillations do not impact the long-term evolution of many of the systems, the oscillations do impact whether a system is categorized

⁵As described previously, as f_D decreases, \mathcal{A} decreases, which causes the Roche lobe to increase and reduces the mass transfer rate.

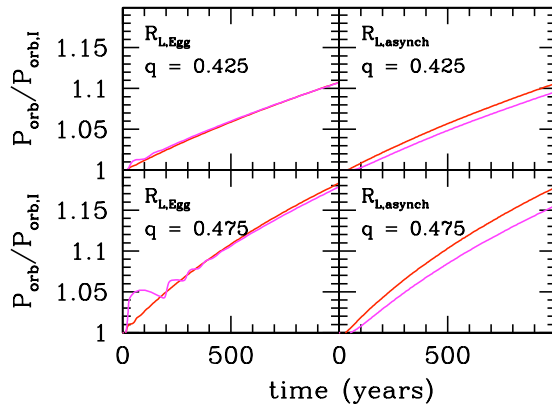


Fig. 11.— Evolution of the orbital period for two different mass ratios. The upper graphs show the evolution for an initial mass ratio of $q = 0.425$ ($M_D = 0.34 M_\odot$ and $M_A = 0.8 M_\odot$) and the lower graphs show an initial mass ratio of $q = 0.475$ ($M_D = 0.38 M_\odot$ and $M_A = 0.8 M_\odot$). The left-hand panel shows evolution using $R_{L,Egg}$ and the right-hand panel shows evolution using $R_{L,asynch}$. As in Figure 10, the red plots show evolution for an initial synchronization time-scale of $\tau = 10$ yrs and the magenta plots show the evolution for $\tau = 40$ yrs.

as sub-Eddington or super-Eddington or whether it reaches unstable levels of mass transfer. In the case of the system illustrated in Figures 8 and 9, the oscillations cause the system briefly to become super-Eddington, while the system would remain sub-Eddington in the absence of oscillations.

In general, as the mass transfer rates spike initially under the $R_{L,Egg}$ calculation before ultimately settling to the $R_{L,asynch}$ value, it may reach super-Eddington or unstable levels, while, in the $R_{L,asynch}$ case, the mass transfer rate may remain stable instead of super-Eddington, or super-Eddington instead of unstable. This explains the lack of unstable black systems in Figure 5 compared to Figure 3. For the systems shown in Figure 3, the oscillations in the orbital parameters arising from the use of $R_{L,Egg}$ may cause the mass transfer rate to reach artificially high values before the oscillations relax, leading to the large population of black systems at the top of the figure. Meanwhile, since using $R_{L,asynch}$ damps the oscillations, the mass transfer rate is able to stay below the limit for stability of $0.01 M_\odot/\text{yr}$.

Both Marsh2004 and Gokhale2007 noted the presence of oscillations in the orbital parameters near the boundary between stable and un-

stable systems. These analyses observed that, for such systems, small changes in the synchronization time-scales and in the mass ratio will cause changes in the frequency and amplitude of the oscillations. Figures 10 and 11 show the evolution of the orbital period for various synchronization time-scales and mass ratios, respectively, using both $R_{L,Egg}$ and $R_{L,asynch}$ to calculate the size of the Roche lobe. These figures confirm the observations of Marsh2004 and Gokhale2007 that the amplitude and frequency of the oscillations is dependent upon both the mass ratio and the synchronization time-scale.

The left-hand panel of Figure 10 illustrates that the amplitude of the oscillations increases with increasing initial synchronization time-scale, while the frequency of the oscillations decreases. These oscillations can be explained as follows: Once mass transfer begins, if the system is unstable or nearly unstable, the time-scale for changes in the mass transfer rate becomes greater than the time-scale at which the semi-major axis increases due to tides. As a result, \dot{M}_D increases rapidly and the accretor spin increases significantly. The result is a large asynchronicity between the accretor, the orbit, and the donor. As the orbital separation increases due to the effect of tides, \dot{M}_D decreases, until the timescale for changes in the mass transfer rate becomes less than the time-scale at which the semi-major axis increases due to tides. At this point, tides are able to redistribute angular momentum from the spin of the accretor back into the orbit. If enough angular momentum is transferred back into the orbit, the donor becomes detached. Once tides effectively re-synchronize the spins of the stars with the orbit, gravitational wave losses act to bring the binary back into contact, and the entire cycle repeats.

The right-hand panel of Figure 10 demonstrates that, for this particular mass ratio, the oscillations are not present when using $R_{L,asynch}$ to calculate the size of the Roche lobe. Furthermore, the right-hand panel illustrates that, in the absence of oscillations, the orbital period, and therefore, the semi-major axis increases more rapidly for lower τ values of the synchronization timescale. For lower τ values, the tidal coupling is stronger, which means spin angular momentum is able to be re-distributed more efficiently, which allows the semi-major axis to remain larger compared to the

semi-major axis of systems evolved using higher values of τ .

Figure 11 demonstrates the effect of mass ratio upon the amplitude of the oscillations. As Gokhale2007 observes, we see that for a fixed τ value, a lower mass ratio (top two graphs of Figure 11) yields oscillations of lower amplitude compared to a higher mass ratio (lower two graphs of Figure 11). In Figure 3, we see that switching from a mass ratio of 0.475 to 0.425 moves us away from the boundary which separates super-Eddington systems from stable systems. This demonstrates that, in general, as we move away from the stability boundary, the oscillations are reduced.

The two right-hand panels of Figure 11 show the evolution using $R_{L,asynch}$ for the Roche lobe. This again demonstrates that oscillations are not present when the Roche lobe depends on the asynchronicity between the donor and orbit.

5. Conclusions

We have studied the long-term evolution of DWD binary systems undergoing direct-impact mass transfer, including the effects due to mass transfer, gravitational radiation, and tidal forces arising from asynchronicity between the donor, accretor, and the orbit. We implemented the ballistic mass-transfer treatment developed in (Sepinsky et al. 2010) to calculate the changes to orbital parameters during direct-impact mass transfer. By implementing this method, we found that the number of stable DWD systems increased for both weak and strong tidal coupling compared with the results of Marsh2004 and Gokhale2007, as shown in Figures 2 and 3.

For the first time, we also account for the modification of the Roche-lobe size due to the asynchronicity of the donor. As a result, we find that the number of stable systems increases, particularly for the case of strong tidal coupling, as shown in Figures 5 and 6. When not accounting for the asynchronicity effects on the Roche-lobe size, we reproduce the oscillations in the orbital parameters first noted by Gokhale2007. We found that, when the size of the Roche lobe was permitted to vary with donor asynchronicity, these oscillations were dampened, as shown in Figure 8. We conclude that the oscillations created when using the Eggleton approximation for the Roche lobe calcu-

lation create artificially high mass transfer rates which leads to an artificially high number of super-Eddington and unstable systems. By eliminating the oscillations, our treatment yields a higher number of sub-Eddington and stable systems.

We expect systems which are stable throughout our calculations (red systems in Figures 2, 3, 5, and 6) to be AM CVn progenitors. As a result of the increase in stable systems shown here compared to previous analyses, we conclude that DWD evolution may be a more likely avenue for the creation of AM CVn than previously expected.

In future analyses, we intend to investigate the case of initially eccentric binaries with asynchronous component stars, as we expect there may be a significant population of DWDs that have not had time to circularize and synchronize by the time mass transfer occurs (Willems et al. 2007). Additionally, we intend to implement a treatment of disc accretion so that we can track the evolution of the DWD systems through all types of accretion processes.

6. Acknowledgements

KK and VK acknowledge support from Northwestern University that made this project possible. VK is also grateful for the hospitality of the Aspen Center for Physics. This work used computing resources at CIERA funded by NSF PHY-1126812.

REFERENCES

- Bours, M.C.P. et al. (2014), MNRAS, 438, 3399.
- Burkart, J., Quataert, E., and Arras, P. 2014, MNRAS, 443, 2957.
- Campbell, C. G. 1984, MNRAS, 1984, 433.
- Chandrasekhar, S. 1967, An Introduction to the Study of Stellar Structure. Dover, New York.
- Eggleton, P. P. 1983, ApJ, 268, 368.
- D’Souza, M. C. R., Motl, P. M., Tohline, J. E., and Frank, J. 2006, ApJ 643, 381.
- Frank, J., King, A., and Raine, D. 2002, Accretion Power in Astrophysics. Cambridge University Press, Cambridge.
- Fuller, J. and Lai, D. 2014, MNRAS, 444, 3488.
- Galassi, M. J. D., Theiler, J., Gough, B., Jungman, G., Booth, M., and Rossi, F. 2006, GNU Scientific Library Reference Manual (2nd Ed.) (Network Theory Ltd.)
- Gokhale, V., Peng, X. M. and Frank, J. 2007, ApJ 655, 1010.
- Han, Z. and Webbink, R. F. 1999 A and A, 349, L17.
- Hils, D., Bender, P.L. and Webbink, R. F. 1990, ApJ 360, 75.
- Hils, D. and Bender, P.L. 2000, ApJ 537, 334.
- Hut, P. 1981, A and A 99, 126.
- Kruszewski, A. 1963, Acta Astronomica, 13, 106.
- Landau, L. D. and Lifshitz, E. M. 1975, The Classical Theory of Fields. Pergamon Press, Oxford.
- Maoz, D., Mannucci, F., and Nelemans, G. 2014, AARA, 52, 107.
- Marsh, T. R., Dhillon, V. S. and Duck, S. R. 1995, MNRAS, 275, 828.
- Marsh, T. R., Nelemans, G. and Steeghs, D. 2004, MNRAS, 350, 113.
- Motl, P. M., Frank, J., Tohline, J. E. and D’Souza, M. C. R. 2007, ApJ, 670, 1314.
- Nather, R. E., Robinson, E. L. and Stover, R. J. 1981, ApJ, 244, 269.
- Nelemans, G., Yungelson, L. R. and Portegies Zwart, S. F. 2001, A and A 375, 890.
- Paczynski, B. and Sienkiewicz, R. 1972, Acta. Astron., 22, 73.
- Plavec, M. 1958, Mémoires de la Société Royale des Sciences Liège, 20, 411
- Savonije, G. J. 1978, A and A, 62, 317.
- Sepinsky, J., Willems, B. and Kalogera, V. 2007, ApJ, 660, 1624.
- Sepinsky, J., Willems, B., Kalogera, V., and Rasio, A.F. 2010, ApJ, 724, 546.
- Sepinsky, J. and Kalogera, V. 2014, ApJ, 785, 157.
- Shen, K. 2015, ApJL, submitted.
- Soberman, G.E., Phinney, G.S., and van den Huevel, E. P. J. 1997, A and A, 327, 620.
- Tutukov, A. and Yungelson, L. 1996, MNRAS, 280, 1035.
- Valsecchi, F., Farr, W.M, Willems, B., Rasio, F.A., and Kalogera, V. 2013, ApJ, 773, 39.
- Verbunt, F. and Rappaport, S. 1988, ApJ, 332, 193.
- Webbink, R. F. 1977, ApJ, 211, 486.
- Webbink, R. F. 1984, ApJ, 277, 355.
- Willems et al. 2007, ApJ, 665, L59.
- Woosley, S. E. and Weaver, T. A. 1986, ARAandA, 24, 205.

This 2-column preprint was prepared with the AAS L^AT_EX macros v5.2.